On Strengthening of the Solar f-mode Prior to Active Region Emergence Using the Fourier-Hankel Analysis

Waidele[1,2] •• · Roth[1] •• · Singh[3] •• · Käpylä[4] ••

Abstract Recent results of Singh et al. (2016) show that the emergence of an active region (AR) can be seen in a strengthening of the f-mode power up to two days prior of the region's formation. In the original work, ring diagram analysis was used to estimate the power evolution. In this study, we make use of the Fourier-Hankel method, essentially testing the aforementioned results with an independent method. The data is acquired from SDO/HMI, studying the ARs 11158, 11072, 11105, 11130, 11242 and 11768. Investigating the total power as a function of time, we find a similar behavior to the original work, which is an enhancement of f-mode power about one to three days prior to AR emergence. Analysis of the absorption coefficient α, yielded by a Fourier-Hankel analysis, shows neither absorption ($\alpha > 0$) nor emission ($\alpha < 0$) of power during the enhancement. Finding no changes of the absorption coefficient (i.e. $\alpha = 0$) is an important result, as it narrows down the possible physical interpretation of the original f-mode power enhancement, showing that no directional dependence (in the sense of inward and outward moving waves) is present.

Keywords: Sun, helioseismology; Sun, activity; Sun, magnetic fields

1. Introduction

Finding ways to reliably predict the emergence of active regions is an important application of solar physics, as it allows for the ability to forecast some aspects of space weather. Solar eruptive phenomena embrace a variety of eruptions, including flares, solar energetic particles, and radio bursts This is due to the fact that active regions act

✉ Waidele
mwaidele@stanford.edu

1   Leibniz-Institut für Sonnenphysik (KIS), Schöneckstrasse 6, 79104, Germany

2   W. W. Hansen Experimental Physics Laboratory, Stanford University, Stanford, CA 94305-4085, USA

3   Inter-University Centre for Astronomy & Astrophysics, Post Bag 4, Ganeshkhind, Pune 411 007, India

4   Georg-August-Universität Göttingen, Institut für Astrophysik, Friedrich-Hund-Platz 1, 37077 Göttingen.

as hosts to almost all solar eruptive phenomena, such as flares, radio bursts and coronal mass ejections (Webb & Howard, 2012; Temmer, 2021). In the context of helioseismology, it has been shown in the past that active regions strongly influence many solar properties measure with helioseismic methods (Rajaguru, 2001; Braun & Birch, 2006; Schunker et al., 2013; Rijs et al., 2015), even before the appearance of a strong magnetic field in surface magnetograms (Hartlep, 2009). Emerging active regions have been investigated in the past by means of time-distance helioseismology (Ilonidis, 2011), down to a depth of 75 Mm. In terms of actual precursor signals, a retrograde flow with an amplitude of $100\,\mathrm{m/s}$ roughly 2 hours prior to emergence has been observed (Schunker et al., 2016), while subsurface flows remain weak (on the order of $1\,\mathrm{m/s}$, not larger than $15\,\mathrm{m/s}$) and obfuscated (Hanasoge, 2008; Birch et al., 2013). Other fruitful studies involving the fundamental mode (f-mode) yielded many results regarding shallow (usually only a few Mm) subsurface magnetic fields (Hindman et al., 2004). The theoretical work of Singh et al. (2014, 2020) shows that f-mode frequencies, as well as its amplitude, are sensitive to subsurface magnetic fields. As many details about the build up and the emergence of active regions, as well as their subsurface flows and structure remain uncertain (Gizon et al., 2009; Moradi et al., 2010), studying f-mode variability in the presence of active regions is a promising method to learn about the solar dynamo (Charbonneau, 2020) and subsurface solar magnetism more specifically (Hanasoge, 2008; Felipe et al., 2012).

This study builds on the observations of Singh et al. (2016), who reported a systematic strengthening of f-mode power, prior to the emergence of an active region. We employ a Fourier-Hankel analysis to first estimate the power evolution aiming to test the aforementioned observations with an independent method, and secondly, to calculate the absorption coefficient α, to potentially link these results to earlier studies. A Fourier-Hankel analysis was first applied in the context of helioseismology by Braun et al. (1987), in order to investigate the power absorption by sunspots. The Fourier-Hankel method was further used and refined in the context of local helioseismology (Couvidat, 2013; Felipe et al., 2014). It has been useful specifically in investigations of power evolution in solar surface magnetism (Fan et al., 1995; Lindsey & Braun, 1999).

Our work relies on Dopplergrams recorded by HMI (Schou et al., 2012) and the data processing reported in the original work of Singh et al. (2016). We test the hypothesis that there is an initial enhancement of f-mode power 1 to 3 days prior to the emergence of an active region, followed by the well established power reduction due to the sunspot being present. Simultaneous to the reduction of power, an increase in absorption ($\alpha > 0$) will follow. Therefore, calculating α during the initial power enhancement can either result in emission (decrease of the absorption coefficient, $\alpha < 0$), which will let us make a connection to the sunspot-power behavior, or a result of zero absorption ($\alpha = 0$) suggesting another, potentially unknown, mechanism to be present.

At first we will go over data acquisition and treatment in Section 2, discussing similarities and differences compared to the original work. Second, details regarding the Fourier-Hankel method applied here will be discussed in Section 3. Our results will be presented in Section 4, while discussion and conclusions are shown in Section 5.

2. Data Acquisition and Treatment

The data preparation is designed to be as similar as possible to that described in Singh et al. (2016), albeit a different helioseismic method was used. As a first step for the analysis, we track AR 11158 starting prior to its emergence on 2011.02.14 with *mtrack* (Bogart, 2007), using the Snodgrass-rate as tracking rate (Snodgrass & Ulrich, 1990). Furthermore, for every frame the line-of-sight component of both observer velocity and solar rotation are removed. The contributions of granulation to the velocity signal are reduced by applying a running difference, yielding a from now on labeled corrected velocity signal v. In addition to the magnetically active region, a quiet-Sun control region with the same tracking rate and initial position but on the opposite hemisphere is tracked. Thus, for each active region that is tracked with starting point (x, y) (representing longitude, latitude), the corresponding quiet-Sun starting point is given by $(x, -y)$. Let us call this quiet control region as QS 11158, which corresponds to the AR 11158. The B_0-angle at that time is $-6.72°$, which affects the measured surface velocity to some degree, although it does so in a uniform manner concerning northern and southern hemisphere. All other regions (ARs 11072: $t_{\mathrm{AR}} = 2010.05.23$, 11105: $t_{\mathrm{AR}} = 2010.08.03$, 11130: $t_{\mathrm{AR}} = 2010.11.29$, 11242: $t_{\mathrm{AR}} = 2011.06.29$ and 11768: $t_{\mathrm{AR}} = 2013.06.14$) are tracked, similarly to Singh et al. (2016). We take the same definition of AR emergence time t_{AR} as in the original work. Each active region is required to be isolated, meaning no significantly strong magnetic field appears in its vicinity during the full tracking period. Furthermore, all regions should emerge close to the central meridian, such that the region can be observed up to three days, before and after. Using data from cycle 24 only, these requirements lead to a naturally small sample size (a total of six in this case). Increasing the sample can be achieved by considering non-isolated ARs. In this work however, we will restrict ourselves to isolated regions, preferring 'best case' scenarios over a larger amount of data. A snapshot of AR 11158 in a helioprojective coordinate frame is shown in Figure 1, its corresponding quiet-Sun control region (QS 11158) is shown in Figure 2. Note that we opted to show Magnetograms here for visualization purposes, since the extent of the magnetically active region is easier to see. Otherwise Dopplergrams are used throughout the analysis.

Tracking yields five days of 8 hour long 1024 pixel×1024 pixel-data cubes at a cadence of 45s and a map scale of $0.365\,\mathrm{Mm}\,(= 0.03°)$. Each of these 8 hour cubes represents one data point of f-modal power, as we will see in the further analysis. All data cubes contain Postel-projected (see right panels of Figure 1 & 2) Dopplergrams in a heliographic longitude-latitude grid, i.e. $v(x, y, t)$. After performing a Fourier-transform, we select data at $k_x = 0$, i.e. $V(k_x = 0, k_y, \nu)$. Here, V is the Fourier-transform of v, k_x represents the longitudinal component of the wavenumber $\boldsymbol{k}$, while k_y represents the latitudinal component and finally ν is the frequency. Afterwards, all data within a certain annulus are considered, as shown in Figure 1. The $k_x = 0$ selection is made to be in accordance with Singh et al. (2016). Its benefits are first and foremost to reduce the total amount of data and can be understood as a customary procedure, equivalent to a longitudinal average, yielding the thus obtained mean power variation in our analysis.
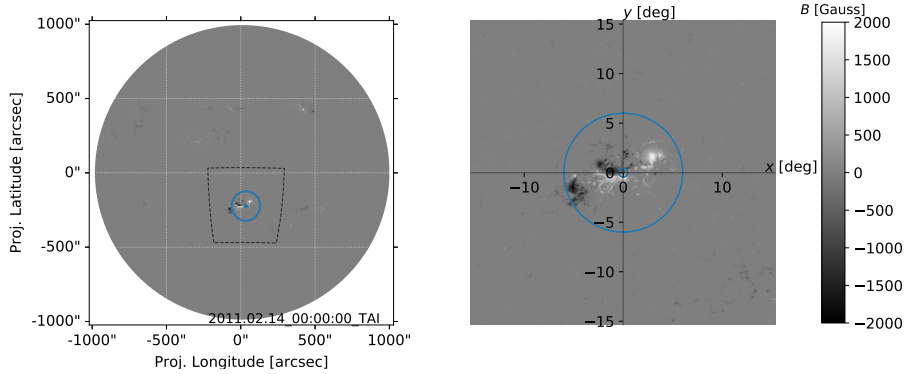
Figure 1. Magnetogram of AR 11158 in helioprojective full disk view (left) and zoomed, heliocentric view (right) during emergence on 2011.02.13, 00:00, displaying the line-of-sight component of the magnetic field. Black dashed lines mark the full tracked area while blue circles highlight the data that is selected for further analysis. The right panel contains the Postel-projected map from the tracked area marked in the left panel.
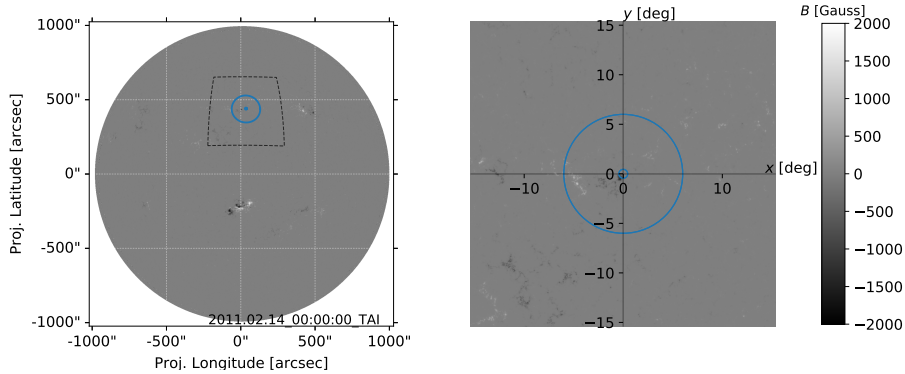

Figure 2. Magnetogram of the quiet-Sun region corresponding to AR 11158 (i.e. QS 11158) in helioprojective full disk view (left) and zoomed, heliocentric view (right) during emergence on 2011.02.13, 00:00. As remarked, this region is tracked simultaneously to AR 11158, but on the opposite hemisphere. An apparent offset from the equator ($y = 0$) can be seen, which is due to the non zero B_0-angle.

3. Fourier-Hankel decomposition

The decomposition method used here is described in detail in Braun et al. (1987) & Gizon & Birch (2005). After Fourier transforming the velocity amplitudes $v(x, y, t)$ of all Dopplergrams within a given annulus (Figure 1 & 2), we select $k_x = 0$ as mentioned and interpolate the resulting signal onto a radial grid. This allows us to further truncate the data, leaving only signals within an annulus, covering the direct vicinity of the (not yet emerged) active region. The annulus (defined by two circles with radii $r_\mathrm{inner}, r_\mathrm{outer}$) has the dimension $r_\mathrm{inner}, r_\mathrm{outer} = (15 \text{ pixel}, 200 \text{ pixel}) = (5.48, 73.07)$ Mm, yielding a grid-spacing of $\Delta\ell = 59.50$. The choice of this small annulus was made since we will deal with very small scale oscillations in the analysis ($\ell \in [1200, 2000]$)

and thus sensitivity to short wavelengths is required. In previous analysis that applied the Fourier-Hankel method, the magnetic region is usually dropped to exclude direct effects of the sunspot to the velocity signal (Braun et al., 1987; Fan et al., 1995). Such direct effects include degrading of the Doppler signal by distorting the atomic line and suppressing oscillations, but also contributions to the line-of-sight velocity by the moat-flow or other surface flows. Here we don't have to worry about direct effects, since we observe the velocity signal prior to the emergence of the active region. In turn, this means that any analysis after the emergence is using velocity signals corrupted by the sunspot. The above mentioned interval of ℓ is expected to show f-mode strengthening prior to the emergence of an active region (Singh et al., 2016), and has been shown to exhibit power enhancement due to a localized subsurface magnetic concentration in simulations Singh et al. (2020). For truncating, a spatial Hann-window λ_N (Blackman & Tuckey, 1958) was applied to the data $V(r, t)$ with

$$\lambda_N(n) = 0.5 - 0.5 \cos \left(\frac{2\pi n}{N-1} \right), \tag{1}$$

where N is the sample size ($N = r_{\text{inner}} - r_{\text{outer}} = 185$ for the spatial window and $N = 640$ for the temporal window) and where $0 \leq n < N - 1$. The Hankel decomposition yields the complex time series $a_\ell(t)$ and $b_\ell(t)$ of in- and outgoing waves within the annulus, by making use of the orthogonality of Hankel functions:

$$a_\ell(t) = \frac{\pi L}{2\Delta r} \int_{r_{\text{inner}}}^{r_{\text{outer}}} \lambda_N(r) V(r, t) H^{(2)}(Lr) r dr, \tag{2}$$

$$L = \sqrt{\ell(\ell+1)} \quad \text{and} \quad \Delta r = r_{\text{inner}} - r_{\text{outer}},$$

whereby $H^{(2)}(Lr)$ is the Hankel function of second kind. For calculating $b_\ell(\nu)$ Equation 2 can be used with the Hankel function of first kind $H^{(1)}(Lr)$. From the complex amplitudes $a_\ell(t)$, $b_\ell(t)$ we calculate the periodograms $P_\ell^{\text{in}}(\nu)$ and $P_\ell^{\text{out}}(\nu)$

$$P_\ell(\nu) = \mathcal{W}_S \left(f_\ell(t) \right), \tag{3}$$

where $\mathcal{W}_S(f)$ denotes calculation of the power-spectrum via Welch's method (Welch, 1967), using again a Hann-window (Eq. 1) and $f_\ell(t)$ is a complex time series representing either $a_\ell(t)$ or $b_\ell(t)$. As is usual for Welch's method, the time-series is further divided into S equally long segments. A window function is applied to each segment, designed in such a way that it overlaps into half of the following segment. This overlap is preferred to avoid bias introduced due to the window function almost eliminating velocity signal close to the edge of individual segments. This techniques results in S individual power spectra, which are then averaged to reduce noise. Here we set $S = 3$, as this appears to be the best trade-off between sufficient frequency resolution and noise reduction in the resulting spectrum. The spectra $P_\ell^{\text{in}}(\nu)$, $P_\ell^{\text{out}}(\nu)$ are obtained for $f_\ell(t) = a_\ell(t)$, $b_\ell(t)$ respectively. Subsequently, we calculate the absorption coefficient (Braun et al., 1987):

$$\alpha_\ell(\nu) = 1 - P_\ell^{\text{out}}(\nu)/P_\ell^{\text{in}}(\nu). \tag{4}$$

Finally, the total power is estimated via

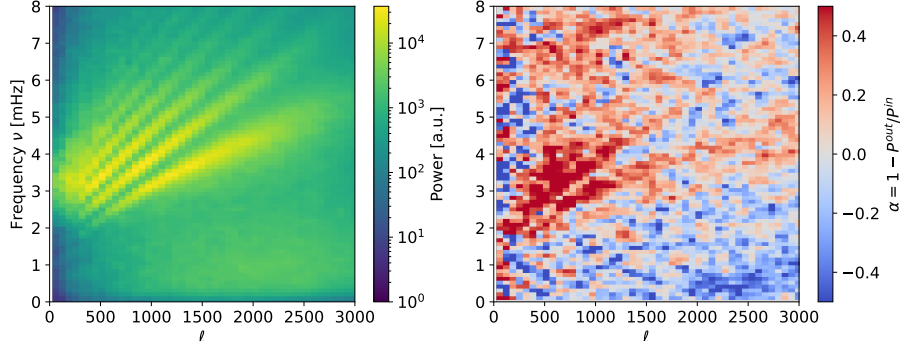$$P_\ell^{\text{tot}}(\nu) = P_\ell^{\text{in}}(\nu) + P_\ell^{\text{out}}(\nu). \tag{5}$$

Figure 3. Power spectrum P^{tot} (left) and absorption coefficient α (right) as a function of harmonic degree ℓ and temporal frequency ν for a duration of 8 hours. As can be seen, the f-mode ridge is well resolved, granulation noise is almost eliminated (due to the running difference) and other background contributions are minimal. In the absorption map, red means power absorption, while blue means power emission. This section of the full time series corresponds to a time after the active region emerged, which explains why absorption along ridges can be seen.

Both $P_\ell^{\text{tot}}(\nu)$ and $\alpha_\ell(\nu)$ are shown in Figure 3. In the left panel we then see the usual ℓ-ν-diagram with multiple ridges. As expected, we see barely any low frequency granulation noise, due to the running difference applied initially. The seemingly low resolution stems from the rather broad grid spacing of $\Delta\ell = 59.50$ and the temporal duration of just 8 hours (the total duration is 5 days which is divided into 8 segments as mentioned). Furthermore, the f-mode "fans out" towards high ℓ (Singh et al., 2014), meaning the line-width increases. This has to be accounted for in the $\ell \in [1200, 2000]$ range, by employing an adequate fit in the following analysis. Comparing the total power to the absorption spectrum (right panel), we also see ridge-like structures. This is due to the active region's emergence towards the end of the observation, which will lead to absorption of power (Braun et al., 1987; Cally & Bogdan, 1997). Another feature is a wide area of weak emission at very low frequencies $\nu < 2$ mHz below the f-mode frequencies and rather large ℓ, seemingly within the range of solar granulation (see for example Couvidat 2013; Waidele et al. 2021) and propagating gravity waves. In this particular frequency range, the absorption coefficient α is rather unreliable, since not a lot of power is present in the first place. Either way, the region is well separated from in the frequency domain from the f-mode ridge, ensuring that such granulation noise does not affect further analysis.

Error estimates are calculated as described in Priestley (1981). The variance of a periodogram P is given as $\text{var}(P) = 4P^2$ and does not depend on the sample size N

(which is a general property of a χ_2^2-distribution). Applying window functions $\lambda(t)$ to the data however, reduces the variance as follows

$$\mathrm{var}(P) = P^2 \frac{\sum_{t=0}^{N} \lambda_N^2(t)}{\sum_{t=0}^{N} \lambda_N(t)} \ . \tag{6}$$

The apodization process also makes the χ^2-distributed periodogram converge towards a Gaussian distribution (enabling the estimation of an actual errorbar). Since we use Hann windows, the variance reduces to $\mathrm{var}(P) = P^2 \cdot 3/4$, with the corresponding error $\sigma_P/P = 0.866$. This is further reduced by averaging over $S = 3$ segments (see Equation 3). Furthermore, performing weighted sums over ℓ and ν as will be shown in the next Section finally yields $\sigma_P/P = 0.133$, or for the absorption α

$$\sigma_\alpha/\beta = 0.188, \tag{7}$$
$$\beta = P^{\mathrm{out}}/P^{\mathrm{in}} \ . \tag{8}$$

This process results in a reliable estimation of errorbars as the spectra P follow approximately Gaussian distributions.

4. Results

To calculate the absorption coefficient α along the f-mode more precisely, we first have to find solid estimates for $P_\ell^{\mathrm{in}}(\nu)$ and $P_\ell^{\mathrm{out}}(\nu)$. For this purpose, we employ a procedure equivalent to that presented in Singh et al. (2016). Thus, we fit the entire spectrum to find the power distribution of the f-mode, using a combination of Lorentz-curves (to describe oscillatory processes within the spectrum) and Gaussian-curves plus constant (to describe background power). Most of the power $P_\ell(\nu)$ within $\ell \in [1200, 2000]$ is made up of contributions from the f-mode ridge, the p_1-ridge and background, such that the most simple model $M(\nu)$ is given by two Lorentz-curves $L_{\mathrm{f}}(\nu) + L_{\mathrm{p},\,1}(\nu)$ plus a single Gaussian $G(\nu)$ plus a constant background c:

$$M(\nu) = L_{\mathrm{f}}(\nu) + L_{\mathrm{p},\,1}(\nu) + G(\nu) + c \tag{9}$$

Although there are notable contributions from higher order p-modes, they barely contribute to the f-mode power distribution itself, such that, for the sake of fit robustness, we do not consider higher orders for our fit function. An example of a fit result for a single value of ℓ (here $\ell = 1556$, exemplary for $P^{\mathrm{in}}(\nu)$) is shown in Figure 4. In Figure 5 we show a comparison of the available power data (also exemplary for $P^{\mathrm{in}}(\nu)$) with the fit results for all spectra $\ell \in [1200, 2000]$.

By making use of the true f-mode spectrum $L_{\mathrm{f}}(\nu)$ we can estimate the energy E_{f} within the f-mode as follows:

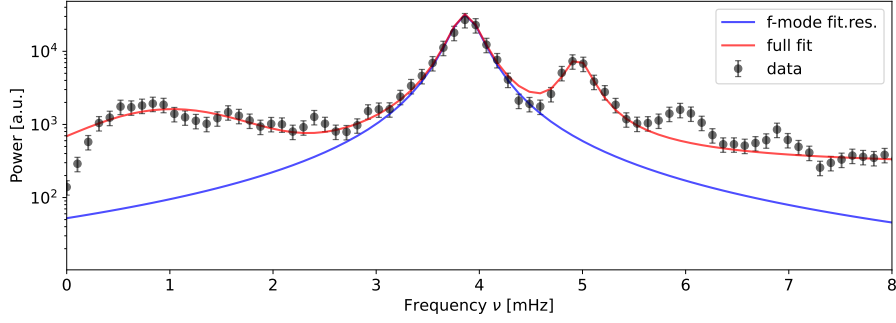$$E_f(\nu) \propto \sum_k k P^{\mathrm{tot}}(\nu), \tag{10}$$

Figure 4. Result of fitting $P_\ell^{\text{in}}(\nu)$ for $\ell = 1556$ for an arbitrary 8 hour segment in logarithmic scale. Black dots represent the data. The red line shows the fit result, using $M(\nu)$ as model function (Eq. 9), whereas the blue line only shows the according result for $L_{\text{f}}(\nu) + c$, i.e. the true f-mode power spectrum plus a static background c.
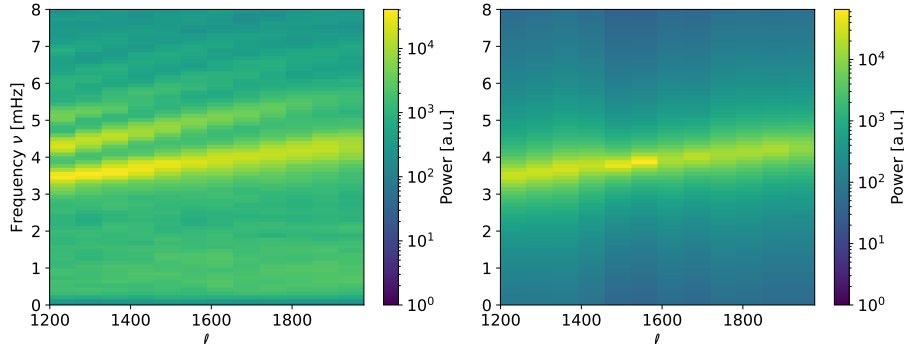

Figure 5. Result of fitting the spectrum around the f-mode, but for all $\ell = [1200, 2000]$ (therefore the same as Same as 4, but for all $\ell = [1200, 2000]$) for an arbitrary 8 hour segment. Left shows the data $P_\ell^{\text{in}}(\nu)$ and right shows the according model attempt using $L_{\text{f}}(\nu)$ to describe the f-mode power spectrum.

therefore representing essentially a weighted sum over $k = \ell/(2\pi R_\odot)$. Still, $E_f(\nu)$ is explicitly given as a function of time $E_f(\nu) = E_f(\nu, \langle t \rangle)$, since we divided the full 6 day time series into $\langle t \rangle = 8$ hour segments. Thus, for a smoother result, we sum over the entire spectrum ν:

$$E_f(\langle t \rangle) = \sum_\nu E_f(\nu, \langle t \rangle) \tag{11}$$

It is important that we recognize that $E_f(\langle t \rangle)$ is not only an explicit function of time, but also an implicit function of longitude, as the tracked region wanders across the solar disk as time passes. This fact will lead to a systematic weakening of oscillatory power when $E_f(\langle t \rangle)$ is measured close to the limb. Solar oscillations are seen in the vertical velocity component, while contributions to horizontal velocities generally stem from granulation. Finally, this causes $E_f(\langle t \rangle)$ to show strong variations along the longitude,

which can be accounted for by using an empirical model ζ (see Singh et al. (2016)), with

$$\zeta(\cos\alpha) = \cos\alpha\,(q + (1-q)\cos\alpha)\,,$$
$$\cos\alpha = \cos\theta\cos\phi, \quad \text{and } q = 0.5\,,$$

(12)

in which θ and ϕ represent the latitude and longitude of the tracked region. Now we can correct $E_f(\langle t\rangle)$ using

$$\widetilde{E_f}(\langle t\rangle) = E_f(\langle t\rangle)/\zeta\,.$$

(13)

Although, the main focus of this work is to calculate power absorption as a function of time $\alpha(\langle t\rangle)$, estimating the energy $\widetilde{E_f}(\langle t\rangle)$ alongside $\alpha(\langle t\rangle)$ is important to allow for direct comparison between the two and shed additional light to the findings of Singh et al. (2016). For the correct estimation of $\alpha(\langle t\rangle)$, we employ a weighted sum over k and a sum over ν for both spectra $P_\ell^{\text{in}}(\nu)$ and $P_\ell^{\text{out}}(\nu)$. A further correction using ζ is not required, since longitudinal dependencies are canceled out when calculating the ratio $P^{\text{out}}/P^{\text{in}}$ as in Equation 4. Note that we only consider a proportional component of $E_f(\langle t\rangle)$ in Equation 10 which means that both energy and power essentially mean the same thing in the context of this work.

The f-mode energy $\widetilde{E_f}(\langle t\rangle)$ and the absorption coefficient $\alpha(\langle t\rangle)$ are both shown for AR 11158 in 6.
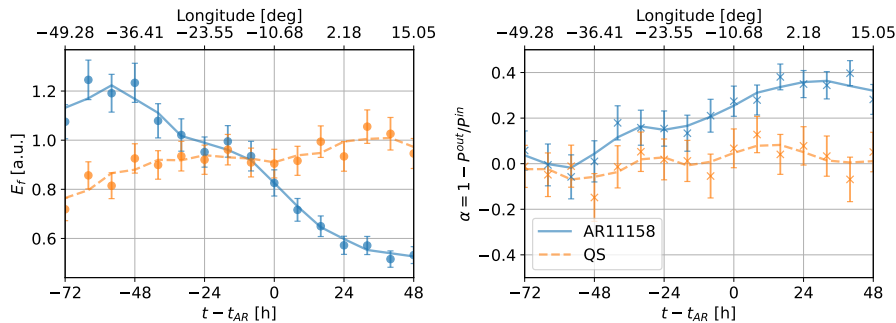

Figure 6. Shown are f-mode energy $\widetilde{E_f}(\langle t\rangle)$ (left) and the absorption coefficient α (right) for all time segments $\langle t\rangle$ minus the emergence time of the active region t_{AR} (namely $t - t_{\text{AR}}$). The blue curve represents data taken from the active region sample, the orange (dashed) curved shows the corresponding quiet-Sun data. Curves are 3-point box-car smoothed, to reveal trends better. The top axis (for both panels) shows the Stonyhurst longitude of the tracked regions.

Interpreting the f-mode energy $\widetilde{E_f}(\langle t\rangle)$ can be done by comparing both measurements for the AR and the corresponding QS region. Regarding the quiet-Sun energy, we can generally expect a constant, smooth distribution, providing an expectation for the 'background'-energy of the entire near side of the Sun at that time. Therefore, any deviations from of the AR distribution from its expected (QS-) distribution indicates additional physics. Following the conclusion of Singh et al. (2016), we expect

a strengthening of $\widetilde{E_f}(\langle t \rangle)$ for the AR, about 1 to 3 days prior to its emergence (i.e. $t - t_{\mathrm{AR}} = 0$). What we observe here, is a significant power excess that can be seen before $t - t_{\mathrm{AR}} < -24$ hours. For the following 4 time segments, the energy remains at nominal values before experiencing a stark reduction It is indeed expected that the total power in the active region is suppressed, due to the power absorption of the emerging active region itself.

Looking at the absorption coefficient α (right panel) for quiet-Sun (orange), we expect $\alpha \approx 0$ at all times, since no (relevant) physical process is actively absorbing or emitting power. As we observe, except for minor deviations, this is indeed the case. In principle, even weak magnetic features corresponding to for example short lived pores can cause momentary increases of α, even for quiet-Sun regions. Concerning negative values, the only few (larger scale) mechanisms known to cause $\alpha < 0$ are acoustic glories (refs) and potentially convective motions (refs).

For the active region (blue), a steady increase in absorption is observed during emergence (and arguably even before that) which is thereby in phase with the drop in $\widetilde{E_f}(\langle t \rangle)$. Most notably, no power emission is detected during the strong power excess at $-72\,\mathrm{h} < t - t_{\mathrm{AR}} < -40\,\mathrm{h}$. This is odd at first sight, although not necessarily unsurprising: Looking at both P^{in} and P^{out} individually, see Figure 7, we find that P^{out} is consistently weaker than P^{in}. For the quiet-Sun region we again, expect a smooth, constant distribution with $P^{\mathrm{in}} = P^{\mathrm{out}}$ for all times which is observed except for minor perturbations. In order to explain the f-mode strengthening in the absence of any power emission ($\alpha < 0$), P^{in} and P^{out} have to increase simultaneously during the strengthening phase of $\widetilde{E_f}(\langle t \rangle)$. This is thus also observed as an enhancement of the total power (the energy) at that time. Interestingly, this type of enhancement is fundamentally different from the power absorption by active regions, in which only one of the power components (P^{out} in this case) is affected, while P^{in} remains unchanged. This behavior calls for a specific investigation with the help of theoretical work (i.e. simulations), to learn the exact evolution of P^{in} and P^{out} during the emergence of an active region.
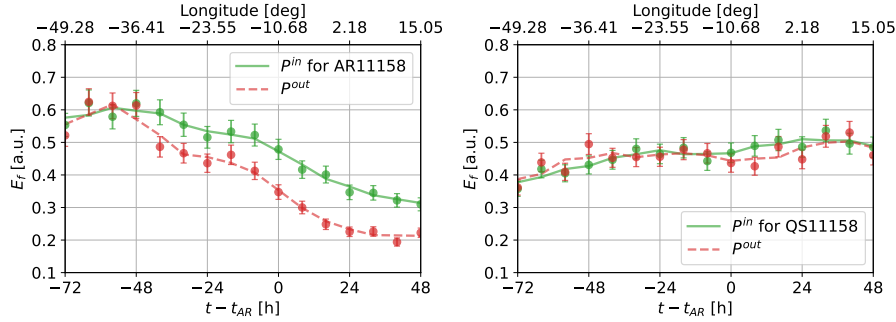

Figure 7. Distributions of power P^{in} (green, solid), P^{out} (red, dashed) as a function of time segment minus active region emergence time $t - t_{\mathrm{AR}}$. The y-axis shows units of f-mode energy, since the estimation procedure for $\widetilde{E_f}(\langle t \rangle)$ (in Eq. 13) was used. Note however that the definition of $\widetilde{E_f}(\langle t \rangle)$ here is more or less interchangeable with power. The left panel shows results for AR 11158, while the right panel shows results for its according quiet-Sun region.

It is important that we convince ourselves of the statistical significance of the power strengthening signal, given the fact that estimations of power spectra tend to be erratic in nature. For this reason, we investigate both the range of errorbars and the data variance around an empirical expectation value, which is shown in Figure 8.
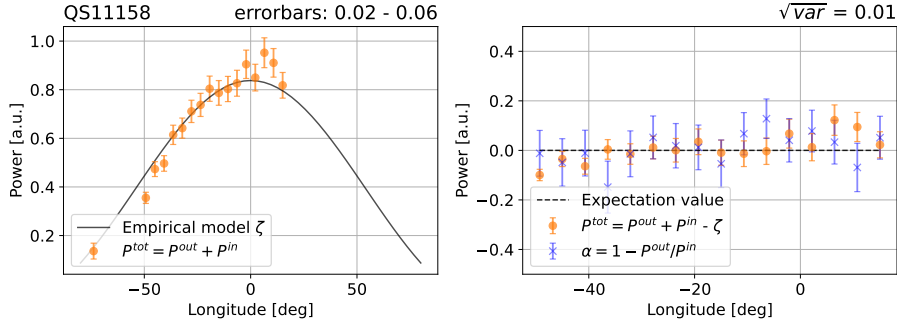

Figure 8. Left: Total power $P^{\mathrm{tot}} = P^{\mathrm{in}} + P^{\mathrm{out}}$ (orange dots, see Eq. 5) and the empirical model ζ (black, see Eq. 12) as a function of longitude, exemplary shown for QS 11158. Right: Variation of $P^{\mathrm{tot}} - \zeta$ around its expected value of 0 as a function of longitude. Shown is also the absorption α (blue crosses) as a function of longitude, to get a feeling for the variation and the errorbars of both quantities. The upper right title of both panels shows the range of errors and the square root of the variance respectively.

From comparing both, it can be seen that approximately $\sqrt{\mathrm{var}} \approx \sigma_P$, indicating that errorbars are at the very least not underestimated.

A set of additional active regions was tracked, according to those in Singh et al. (2016), i.e. AR 11130 (Fig. 9), AR 11072 (Fig. 10), AR 11105 (Fig. 11), AR 11242 (Fig. 12) and AR 11768 (Fig. 13). We repeat the same procedure, leading up to the total power and absorption coefficient as a function of time, and show these in Figures 9 - 13.
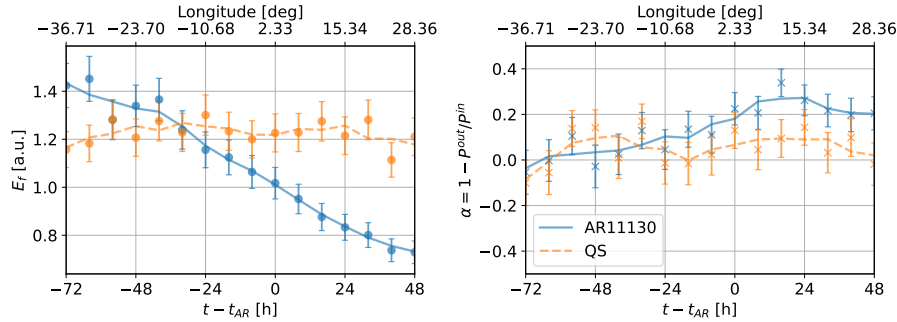

Figure 9. Same as Figure 6, but for AR 11130 and QS 11130.

We observe that the additional active regions overall behave similar to AR 11158. As expected for all ARs, a depression in power at later times occurs, while α increases.
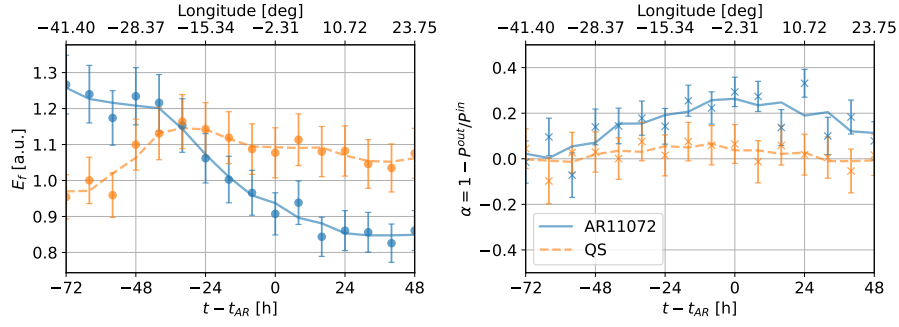
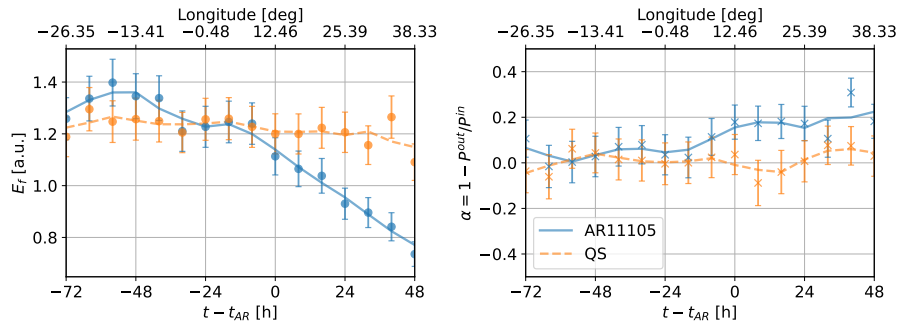**Figure 10.** Same as Figure 6, but for AR 11072 and QS 11072.

Figure 11. Same as Figure 6, but for AR 11105 and QS 11105.

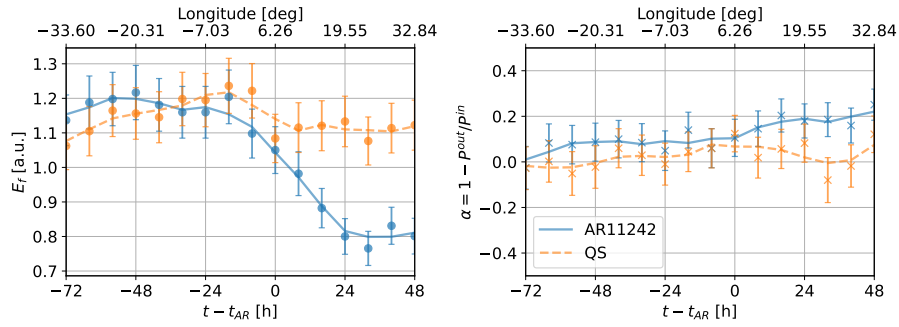**Figure 12.** Same as Figure 6, but for AR 11242 and QS 11242.

While all active regions show a strengthened energy $\widetilde{E_f}(\langle t \rangle)$ compared to their quiet-Sun counterparts, not all of them exhibit significant strengtheningThe main result of α remaining equal to 0 simultaneous to the f-mode energy strengthening is still observed however.
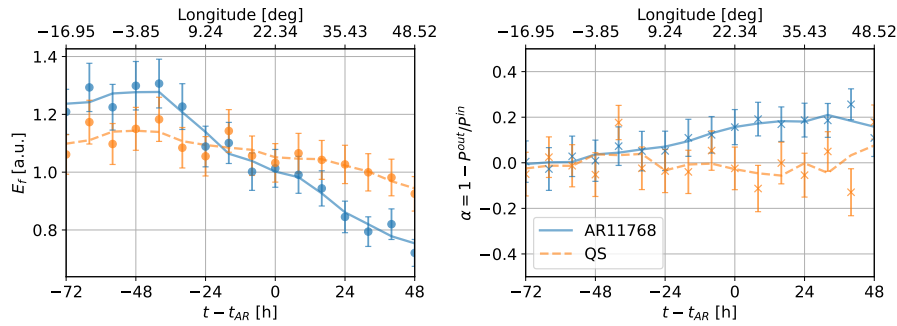
Figure 13. Same as Figure 6, but for AR 11768 and QS 11768.

5. Discussion and Conclusions

We found that the f-mode energy $\widetilde{E_f}(\langle t \rangle)$ for AR 11158 (see Fig. 6) shows a behavior that is qualitatively in line with that reported in Singh et al. (2016), which is a significant enhancement during $-72\mathrm{h} < t - t_{\mathrm{AR}} < -40\mathrm{h}$ prior to AR emergence. The increase in $\widetilde{E_f}(\langle t \rangle)$ is less pronounced for other ARs, especially for AR 11105 (Fig. 11) and AR 11242 (Fig. 12) although still detectable. Furthermore, no such enhancement can be found in the quiet-Sun control regions. Investigations, regarding correlations of this enhancement to the evolution of the surface magnetic flux were carried out in Singh et al. (2016) and yielded inconclusive results. The current method of decomposing the observed Dopplergram is mostly analogous to that used in Singh et al. (2016), but still differs in a few aspects. For one, using the Fourier-Hankel-decomposition to estimate spatial (total) power spectra is different from the standard spatial Fourier decomposition (into sinusoidal functions) used in ring diagram analysis. When calculating $P^{\mathrm{tot}} = P^{\mathrm{in}} + P^{\mathrm{out}}$, we calculate more exactly $\mathcal{W}(a) + \mathcal{W}(b)$ (see Eq. 3), which represents the sum of Bessel functions of first and second kind (Braun et al., 1988). This is mathematically different than the estimation $P^{\mathrm{tot}} = \mathcal{W}(v)$ (v is the velocity signal). However, this difference in power estimation is expected to affect mostly the power magnitude, but not the qualitative distribution. Additionally, the area (annulus, see Fig. 1) we used is smaller, in order to retain some sensitivity of α to oscillations with high harmonic degree ℓ. Overall, the mentioned differences in data processing methods are expected to have a minor influence on the results, as the mathematical way of decomposing the velocity signal is similar, but can still explain the subtlety of f-mode power enhancement, that we find here. Initially we mentioned that P may only be approximately Gaussian distributed, such that it is unclear if σ_P is adequately underestimated. Generally, there are several sources of uncertainty that may contribute to σ_P but which are hardly quantifiable. Examples include instrument-conditioned uncertainties and aforementioned center-to-limb effects. To test the accuracy of σ_P, we estimate the variance of our data P^{tot} (exemplary for a quiet-Sun region), by using an empirical model ζ (see Eq. 12) for its expectation value. For QS 11158, we find values between of approximately 0.01 for $\sqrt{\mathrm{var}(P)}$, while for the estimated error σ_P, values range between $0.02 - 0.06$ (see Fig. 8). An analysis for other QS regions yielded similar

results. It can therefore be assumed that σ_P is accurate, increasing our confidence in the significance of the strengthening of $\widetilde{E_f}(\langle t \rangle)$. Another factor to consider is the aforementioned B_0-angle, which is non-zero in the ARs we investigated. If we assume that P^{tot} for both AR and QS follow the same trend, approximated by ζ, correcting the distribution mostly eliminates this effect, except for a minor distortion in magnitude, which we expect to be much smaller than σ_P however.

Regarding power absorption, it is in general less troublesome to calculate the absorption coefficient α than the total power P^{tot} or energy E, since any result of $P_{\text{out}}/P_{\text{in}}$ automatically corrects most effects of longitudinal (or other time and location dependent) variation, projection effects (center-to-limb) and granulation noise. In our results (see, Figure 6), it is surprising that no emission (i. e. $\alpha < 0$) accompanying the f-mode power strengthening is detected. On the contrary, after the emergence of the AR, its effects on the local velocity field can be seen in total power and α simultaneously. From Figures 9 - 12 we can confirm this behavior. In conclusion, the underlying mechanism of f-mode strengthening as observed in Singh et al. (2016) has thus to be different from the power absorption by sunspots as reported in Braun et al. (1987) and explained in Spruit & Bogdan (1992); Cally & Bogdan (1993); Cally et al. (2003). We thus find with confidence that f-mode strengthening prior to AR emergence is a non-directional (at least in the sense of inward and outward propagation) phenomenon. An idea for a future analysis could include splitting the initial annulus into sectors, to split the power within the annulus into additional directional components (i.e. West-East, North-South).

In conclusion, analysis of total power in the ARs 11158, 11072, 11105, 11130, and 11242 shows similar behavior to that reported in Singh et al. (2016). This can be summarized as follows: Enhancement of f-mode power at high ℓ one to three days prior to AR emergence, followed by depression of f-mode power that sets in just after emergence of the AR, as expected.

Finding the underlying physics of these observations presented and restated here has proven to be difficult, although Singh et al. (2020) found from simulations that the magnetic fields subsurface configuration plays a major role. Our work serves as confirmation of the findings in Singh et al. (2016), additionally yielding original results and conclusions. In combination with the earlier work of Singh et al. (2016), the current results further suggest that high spatial frequency f-mode strengthening needs to be considered as a viable precursor signal of forming ARs. Our results prove that the Fourier-Hankel method not only accompanies the ring diagram analysis in terms of prediction capabilities, but it also provides new insight and information, especially due to the reliability and robustness of the absorption coefficient α to any systematic effect.

References

Birch, A. C. and Braun, D. C. and Leka, K. D. and Barnes, G. and Javornik, B., 2013, *Astrophys. J.*, 762, 131

Blackman, R.B. and Tukey, J.W., 1958, Dover Publications, New York

Braun, D. C. and Birch, A. C., 2006, *Astrophys. J. Lett.*, 647, L187-L190

Bogart, R. S., 2007, Astronomische Nachrichten, 328, 352

Braun, D. C. and Duvall, Jr., T. L. and Labonte, B. J. , 1987, *Astrophys. J. Lett.*, 319, L27-L31

Braun, D. C. and Duvall, Jr., T. L. and Labonte, B. J. , 1988, *Astrophys. J.*, 335, 1015-1025

Cally, P. S. and Bogdan, T. J., 1993, *Astrophys. J.*, 402, 721

Cally, P. S.; Bogdan, T. J., 1997, *Astrophys. J. Lett.*, 486, L67-L70

Cally, P. S. and Crouch, A. D. and Braun, D. C., 2003 *Mon. Not. Roy. Astron. Soc.*, 346, 381-389

Candel, S. M., 1981, Computer Physics Communications, 23, 343-353

Charbonneau, P., 2020, Living Reviews in Solar Physics, 17, 4

Couvidat, S., 2013, *Solar Phys.*, 282, 15-38

Fan, Y. and Braun, D. C. and Chou, D.-Y., 1995, *Astrophys. J.*, 451, 877

Felipe, T. and Braun, D. and Crouch, A. and Birch, A., 2012, *Astrophys. J.*, 757, 148

Felipe, T. and Crouch, A. D. and Birch, A. C., 2014, *Astrophys. J.*, 788, 136

Gizon, L. and Birch, A. C., 2005, Living Reviews in Solar Physics, 2, 6

Gizon, L. and Schunker, H. and Baldner, C. S. and Basu, S. and Birch, A. C. et al., 2009, Space Sci. Rev., 144, 249-273

Hanasoge, S. M., 2008, *Astrophys. J.*, 680, 1457-1466

Hartlep, T. and Kosovichev, A. G. and Zhao, J. and Mansour, N. N., 2009, Astronomical Society of the Pacific Conference Series, 416, 147

Hindman, Bradley W. and Gizon, Laurent and Duvall, Thomas L., Jr. and Haber, Deborah A. and Toomre, Juri, 2004, *Astrophys. J.*, 613, 1253-1262

Ilonidis, Stathis and Zhao, Junwei and Kosovichev, Alexander, 2011, Science, 333, 993

Komm, R. and Morita, S. and Howe, R. and Hill, F., 2008, *Astrophys. J.*, 672, 1254-1265

Lindsey, C. and Braun, D. C., 1999, *Astrophys. J.*, 510, 494-504

Moradi, H. and Baldner, C. and Birch, A. C. and Braun, D. C. and Cameron et al., 2010, *Solar Phys.*, 267, 1-62

Priestley, M. B., 1981, Academic Press, London, 2, 390-406

Rajaguru, S. P. and Basu, Sarbani and Antia, H. M., 2001, *Astrophys. J.*, 563, 410-418

Rijs, Carlos and Moradi, Hamed and Przybylski, Damien and Cally, Paul S., 2015, *Astrophys. J.*, 801, 27

Schou, J. and Scherrer, P. H. and Bush, R. I. and Wachter, R. and Couvidat, S. et al., 2012, *Solar Phys.*, 275, 229-259

Schunker, H. and Gizon, L. and Cameron, R. H. and Birch, A. C. , 2013, *Astron. Astrophys.*, 558, A130

Schunker, H. and Braun, D. C. and Birch, A. C. and Burston, R. B. and Gizon, L., 2016, *Astron. Astrophys.*, 595, A107

Singh, Nishant K. and Brandenburg, Axel and Rheinhardt, Matthias, 2014, *Astrophys. J. Lett.*, 795, L8

Singh, Nishant K. and Raichur, Harsha and Brandenburg, Axel, 2016, *Astrophys. J.*, 832, 120

Singh, Nishant K. and Raichur, Harsha and Käpylä, Maarit J. and Rheinhardt, Matthias and Brandenburg, Axel et al., 2020, Geophysical and Astrophysical Fluid Dynamics, 114, 196-212

Snodgrass, Herschel B. and Ulrich, Roger K., 1990, *Astrophys. J.*, 351, 309

Spruit, H. C. and Bogdan, T. J., 1992, *Astrophys. J. Lett.*, 391, L109-L112

Temmer, Manuela, 2021, Living Reviews in Solar Physics, 18, 4

Waidele, Matthias and Roth, Markus and Vigeesh, Gangadharan and Glogowski, Kolja, 2021, *Astrophys. J.*, 913, 108

Webb, David F. and Howard, Timothy A., 2012, Living Reviews in Solar Physics, 9, 3

Welch, P., 1967, IEEE Trans. Audio & Electroacoust, 15, 70-73